Electronic Supplementary Material (ESI) for Energy & Environmental Science.

Supporting Information for

Self-assembled multilayers direct a buffer interphase toward long-life aqueous zinc-ion batteries

Dongmin Li,[1] Yan Tang,[1] Shuquan Liang,[1] Bingan Lu,[2] Gen Chen,[1,*] and Jiang Zhou[1,*]

[1]School of Materials Science and Engineering, Hunan Provincial Key Laboratory of Electronic Packaging and Advanced Functional Materials, Central South University, Changsha 410083, P.R. China

[2]School of Physics and Electronics, Hunan University, Changsha 410082, P. R. China

E-mail: geenchen@csu.edu.cn; zhou_jiang@csu.edu.cn.

Experimental Section

Materials: L-cysteine (L-cys, BR) was purchased from Shanghai Macklin Biochemical Technology Co., Ltd. Ammonium metavanadate (NH_4VO_3, AR) and N-methyl pyrrolidone (NMP, AR) were purchased from Shanghai Aladdin Biochemical Technology Co., Ltd. Ethanedioic acid dihydrate ($H_2C_2O_4 \cdot 2H_2O$, GR) and zinc powder (AR) were purchased from Sinopharm Chemical Reagent Co., Ltd. Super P (battery grade) and polyvinylidene fluoride (PVDF, battery grade) were purchased from Soochow DoDoChem Technology Co., Ltd. All chemicals were used as received without any further purification.

Preparation of SAM-Zn electrode: Self-assembly of L-cys on Zn anodes was achieved by a simple soaking method. After immersing the ground and polished commercial zinc foil in 0.01M L-cys solution for a certain period, the SAM-Zn was cleaned with deionized water and alcohol to remove excess solution and unstable molecules on the surface, and then dried in a vacuum oven. The thickness of the used zinc foil was 100 μm except for cells with a high DOD (44 μm) and a certain N/P ratio (adjusted according to the capacity of the cathode electrode).

Preparation of SAM-ZnP: Commercial zinc powder was added to 0.01M L-cys solution and stirred for a certain period. The SAM-ZnP was washed with deionized water and alcohol and then dried in a vacuum oven.

Synthesis of $NH_4V_4O_{10}$ cathode material: 1.170 g of NH_4VO_3 was added to 35 mL of deionized water and stirred at 80 °C completely dissolved, and then 1.891 g of $H_2C_2O_4 \cdot 2H_2O$ was slowly added and stirred to obtain a dark blue-green solution. The above solution was transferred to a 50 mL autoclave and placed in an oven at 140 °C for 48 hours. The obtained material was collected and repeatedly washed with deionized water and dried in a vacuum oven at 90 °C for 12 hours.

Preparation of cathode electrode: The cathode electrode consists of $NH_4V_4O_{10}$, conductive super P and PVDF mixed at a mass ratio of 7:2:1 in NMP solvent. The above mixture was uniformly spread on a stainless-steel mesh and dried in a vacuum oven at 90 °C for 12 hours. The effective mass loading of active materials is controlled at around 1.5 mg cm^{-2}. For full cells with low N/P, the above mixture was uniformly spread on a graphite felt to load more cathode active material. The effective mass loading of active materials is controlled at around 4.0 mg cm^{-2}.

Preparation of SAM-ZnP electrode: The SAM-ZnP anode electrode consists of SAM-ZnP, conductive super P and PVDF mixed at a mass ratio of 8:1:1 in NMP solvent. The above mixture was uniformly coated on the copper foil current collector using a doctor blade (120 μm) and dried in a vacuum oven at 90 °C for 12 hours.

Material characterizations: X-ray diffraction (XRD) measurements were carried out on the Rigaku Mini Flex 600 diffractometer with Cu Kα-radiation (λ=1.5418 Å). The surface morphology was characterized by optical microscope (LW750LJT), Atomic force microscope (Bruker Dimension Icon), and scanning electron microscope (SEM, MIRA3 TESCAN, 10 kV). Fourier Transform infrared spectroscopy (FTIR) spectra of the samples were acquired using an FTIR spectrometer (Nicolet 6700, Thermo Electron Science Instruments) to collect vibrational or stretching information of the functional groups of the samples. The wettability of the anode surface was tested with a JY-82B Kruss DSA contact angle measurement system. X-ray photoelectron spectra (XPS) results were performed to investigate the sample valence bond information (ESCALAB 250 Xi X-ray Photoelectron spectrometer, Thermo Fisher). The zinc and organic content in the solution were determined by inductively coupled plasma atomic emission spectrometry (ICP-OES, ICAP7400radial) and Liquid Chromatograph Mass Spectrometer (Shimadzu LCMS-2010), respectively. The time-of-flight-secondary ion mass spectrometry (TOF-SIMS) was used equipped with a 30 keV Bi-cluster liquid metal ion gun to investigate the distributions of the elements (TOF. SIMS 5-100 instrument, IONTOF GmbH).

Electrochemical measurements: 2M $ZnSO_4$ electrolyte, glass fiber separator, Zn/SAM-Zn foil or ZnP/SAM-ZnP anode electrode and $NH_4V_4O_{10}$ cathode electrode matched battery system to assemble CR2025 coin cells and pouch cells. A layer-by-layer process was used to assemble pouch cells with SAM-Zn anode and $NH_4V_4O_{10}$ cathode. The electrode size of pouch cells is 3 cm × 4 cm. The separator size of pouch cells is 3.5 cm × 4.5 cm. The thickness of the separator is 300 μm. The electrolyte addition is controlled to just infiltrate the separator in both the coin cell and the pouch cell. Galvanostatic charge-discharge (GCD) cycling measurements were performed at room temperature at different current densities on a LAND battery tester (LAND CT2001, China). Cyclic voltammetry (CV) curves, chronoamperometry (CA) and electrochemical impedance spectroscopy (EIS) were performed on an electrochemical station (CHI660E, China).

In order to accurately evaluate the kinetics of Zn electrodeposition process, the exchange current density was calculated by the equation:

$$i \approx i_0 \frac{F}{RT} \cdot \frac{\eta}{2}$$

where i and i_0 are running current density and the exchange current density, respectively, F is the Faradic constant, R is the gas constant, T is the Kelvin temperature, and η is total overpotential.

To precisely assess the diffusion capability of Zn^{2+}, the Zn^{2+} transference number of $(t_{Zn^{2+}})$ was evaluated by the equation:

$$t_{Zn^{2+}} = \frac{I_s(\triangle V - I_0 R_0)}{I_0(\triangle V - I_s R_s)}$$

Where ΔV is the applied polarization voltage (10 mV), I_0 and R_0 represent the initial current and resistance, and I_s and R_s are the steady-state current and resistance, respectively.

The electrochemical impedance spectroscopy (EIS) at different temperatures from 20 to 60 °C was used to elaborate on the Zn^{2+} desolvation and transport behavior, which can be calculated according to Arrhenius equation:

$$\frac{1}{R_{ct}} = A \exp\left(-\frac{E_a}{RT}\right)$$

where R_{ct}, A, R, E_a, and T represent the interfacial resistance, pre-exponential factor, the gas constant, activation energy, and temperature, respectively.

Computational methods: The density functional theory (DFT) was carried out using Vienna Ab-initio Simulation Package (VASP). The projected augmented wave (PAW) potentials were chosen to describe the ionic cores and take valence electrons A cutoff energy of 520 eV was adopted for the plane-wave expansion. We further constructed a 6×6 slab with Zn (002) surface termination to represent the substrate of SAM. The vacuum region was more than 15 Å in distance to avoid interactions between neighboring images under periodic boundary conditions. A 2×2×1 Monkhorst-Pack k-point mesh was utilized for Brillouin zone integration. The convergence tolerance for energy and force was set at 10^{-5} eV and 0.02 eV $Å^{-1}$, respectively. The differential charge density distributions are defined as $\Delta\rho = \rho_{total} - \rho_{SAM} - \rho_{substrate}$ where ρ_{total} is the total charge density of the whole system, ρ_{SAM} is the charge density of ordered SAM, and $\rho_{substrate}$ is the charge density of the substrate.

The simulation of interfacial electric field and Zn^{2+} concentration field distribution was carried out using the simulation software COMSOL Multiphysics 5.6 coupled with tertiary current distribution-Nernst-Planck and deformation geometry physics modules. Activation was performed with an overpotential of 50 mV between the anode and the electrolyte as the initial voltage. The initial Zn^{2+} concentration was set to 2M, and the Zn^{2+} diffusion coefficient in the electrolyte was set to 10^{-10} m^2 s^{-1}. The exchange current densities are given by experimental test results. The simulation results of the interfacial electric field and Zn^{2+} concentration field distribution in this work were collected after 10 s.

Figures and Tables

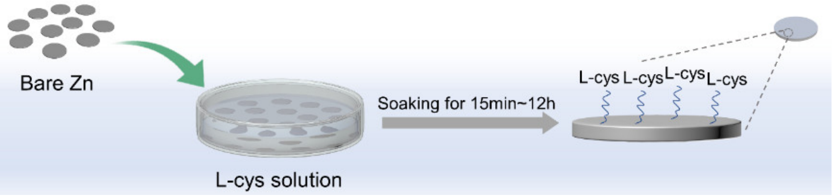

Fig. S1. Preparation process of SAM-Zn.

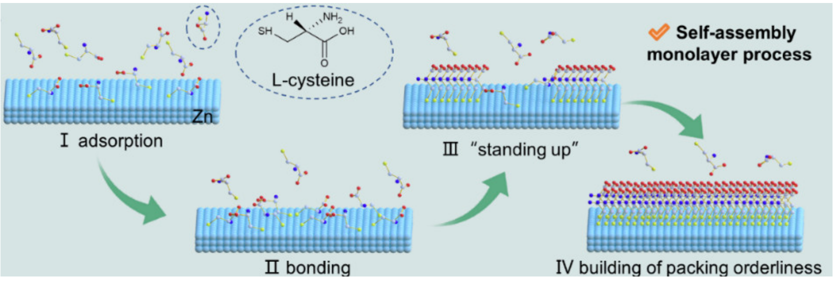

Fig. S2. Schematic illustration of the self-assembly process.

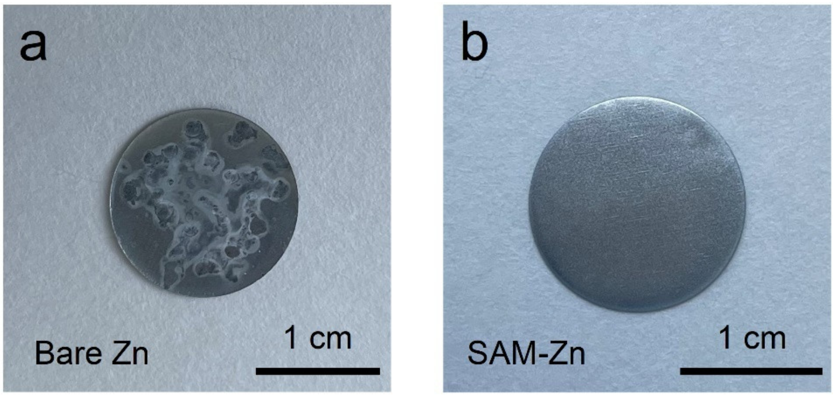

Fig. S3. The optical picture of Zn soaked in a) water and b) L-cys solution for 24 h.

Zinc was soaked in the same way for 24 hours in pure water and L-cys solution. From Fig. S3, it was seen that the phenomenon was completely different, indicating that the modified zinc electrode effectively inhibits corrosion.

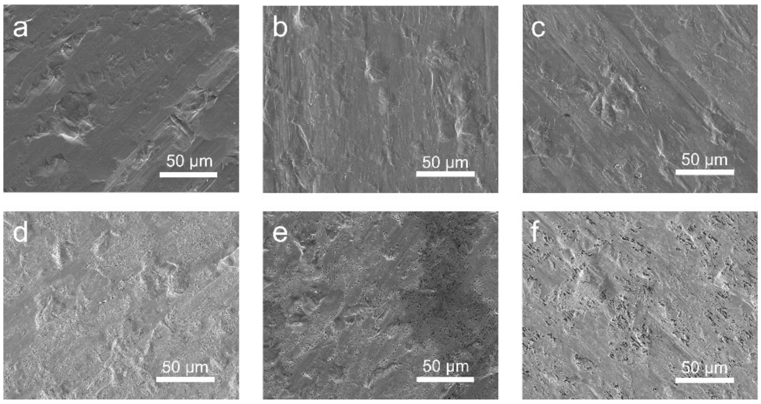

Fig. S4. The SEM images of a) bare Zn and soaked in 0.01M L-cys solution for b) 15 min, c) 1 h, d) 8 h, e) 12 h, and f) 24 h.

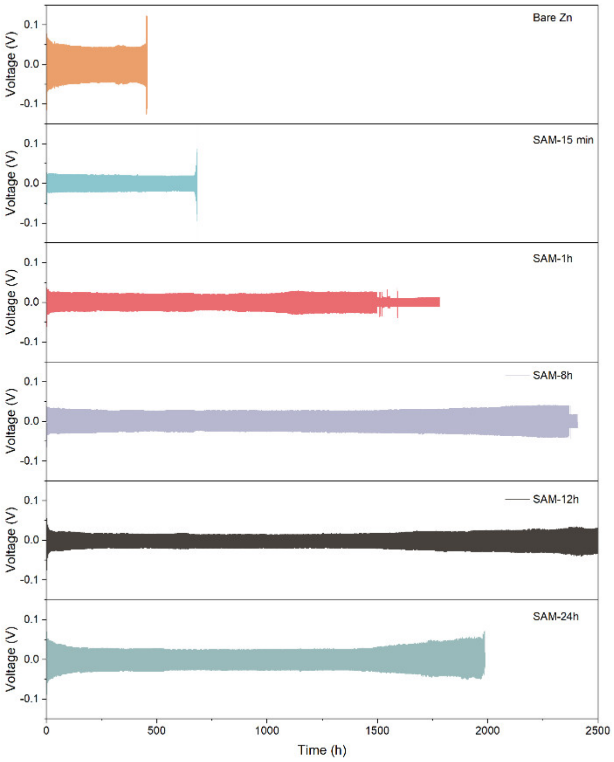

Fig. S5. Long-term cycling performance of SAM-15 min/1 h/8 h/12 h/24 h symmetric cells at 1 mA cm^{-2} with a capacity of 0.5 mAh cm^{-2}.

As displayed in Fig. S5, the electrochemical performance improved even for SAM-15 min and SAM-1 h, which is attributed to the positive effect of SAM. As incubation time is increased to 8 h, SAM-8 h symmetric cell delivers cycling performance of over 2367 h, which is attributed to the effective stacking of the self-assembled molecular layers and the synergistic effect of spatial topology (Fig. S4d). Continuing to increase the incubation time, SAM-12 h exhibits the most excellent long-term cycling performance with a lower hysteresis voltage than the others. However, when the incubation time is increased to 24 h, the SAM-24 h symmetric cell exhibits stable voltage profiles only within 1986 h, which is attributed to the thick self-assembled multilayer and the rougher surface that weakens the positive effect of SAM. Hence, in order to ensure the coverage of the self-assembled structure and the surface topology,12 h (SAM-Zn) was selected as the research object.

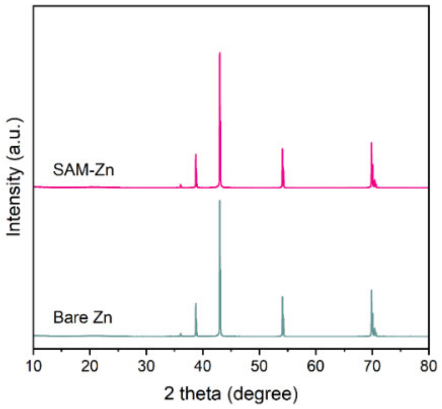

Fig. S6. XRD patterns of bare Zn and SAM-Zn.

None of the peak change is detected in the X-ray diffraction (XRD) pattern, suggesting the trace and amorphous nature.

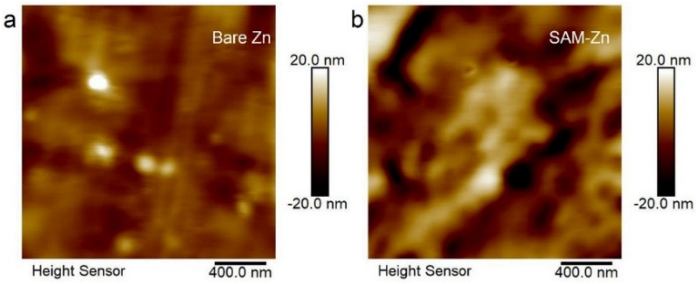

Fig. S7. AFM images of bare Zn and SAM-Zn.

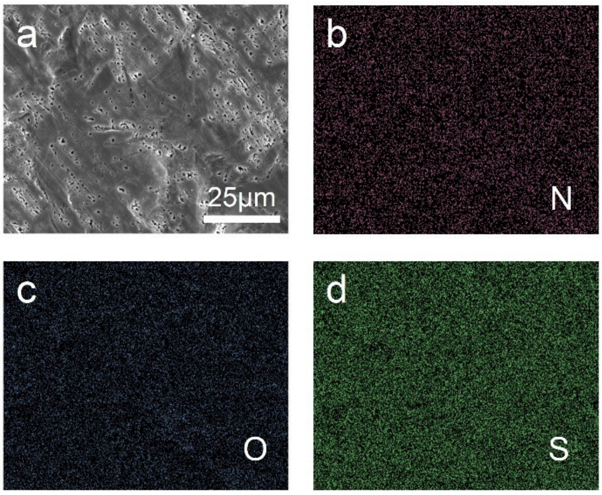

Fig. S8. SEM and EDS images of SAM-Zn.

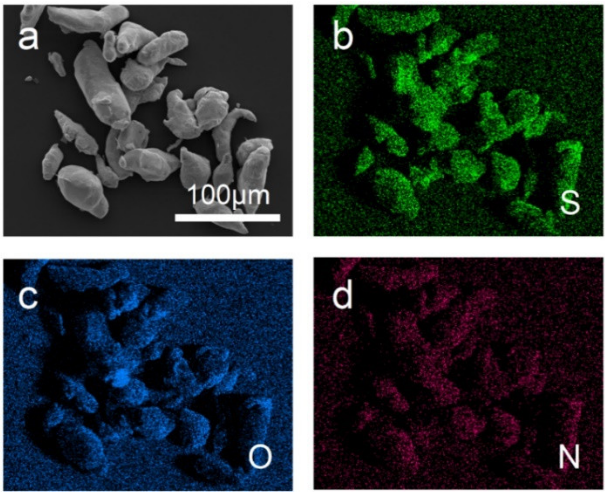

Fig. S9. SEM and EDS images of SAM-ZnP.

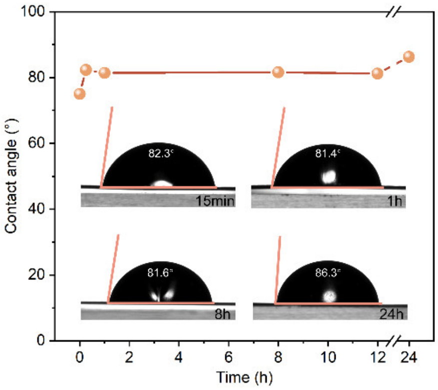

Fig. S10. Contact angles of 2M $ZnSO_4$ electrolyte on SAM-Zn at different preparation times.

The increased contact angle of SAM-24h may be attributed to a visible change in surface.

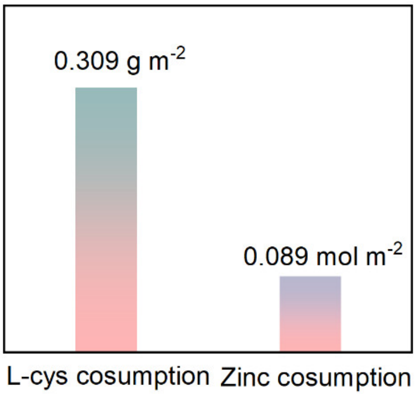

Fig. S11. The consumption of L-cys and Zn during the self-assembly process.

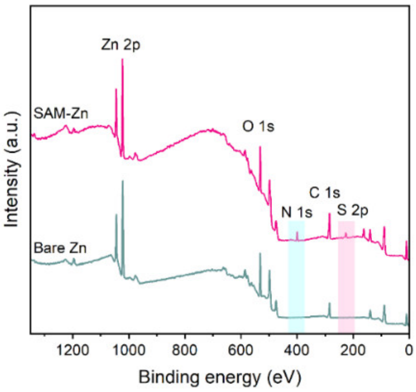

Fig. S12. XPS of bare Zn and SAM-Zn.

The XPS spectra present the typical peaks at S 2p (163 eV), C 1s (285 eV), N 1s (400 eV), and O 1s (532 eV), respectively.

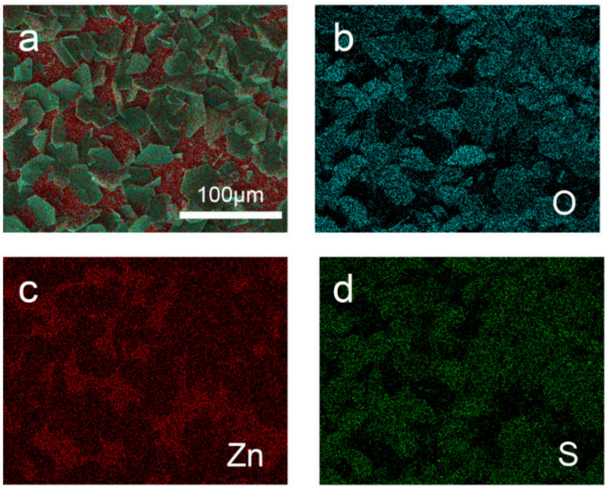

Fig. S13. EDS images of bare Zn after being soaked in the 2M $ZnSO_4$ electrolyte for 6 days.

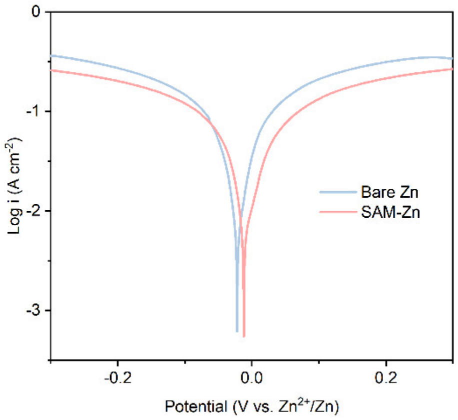

Fig.S14. Linear polarization curves generated for bare Zn and SAM-Zn electrodes in 2M $ZnSO_4$.

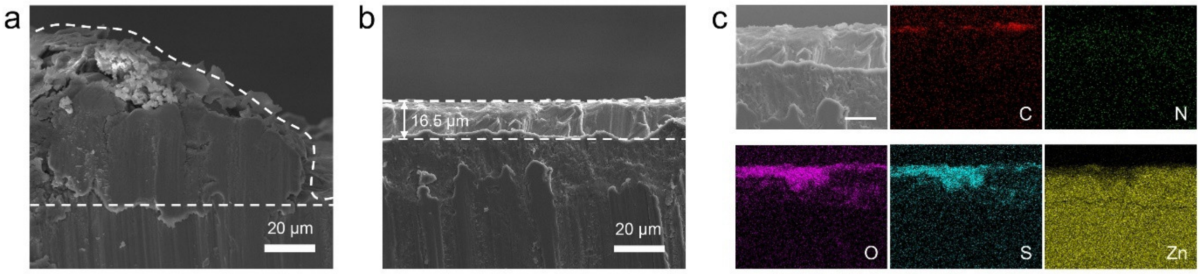

Fig.S15. Cross-sectional SEM image of the Zn deposition on the a) bare Zn, b) SAM-Zn and c) corresponding EDS at a current density of 5 mA cm^{-2} with capacity of 10 mAh cm^{-2}.

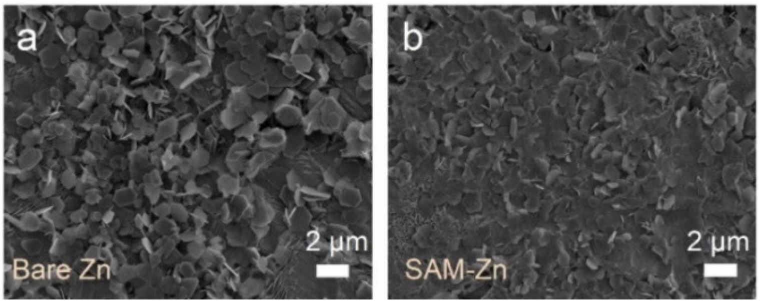

Fig. S16. SEM images of bare Zn and SAM-Zn after one cycle.

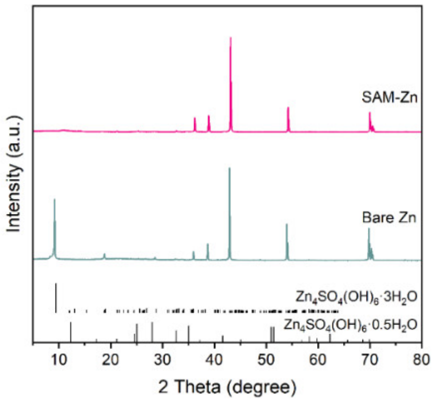

Fig. S17. XRD patterns of bare Zn and SAM-Zn after 100 cycles.

Compared with the bare Zn anode, the SAM-Zn anode exhibits a remarkable effect in suppressing side reactions during electrochemical cycling.

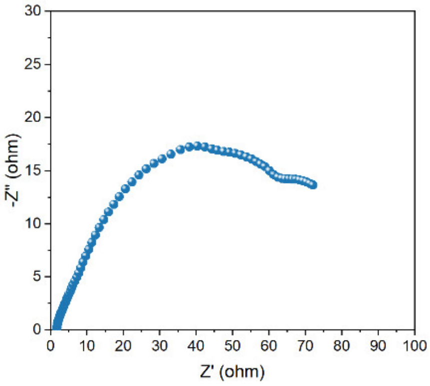

Fig. S18. EIS of SAM-Zn after 200 cycles.

Fresh zinc exposure resulted in a noticeable decline of R_{ct} after cycling, which further prove that no soft short circuit has occurred.

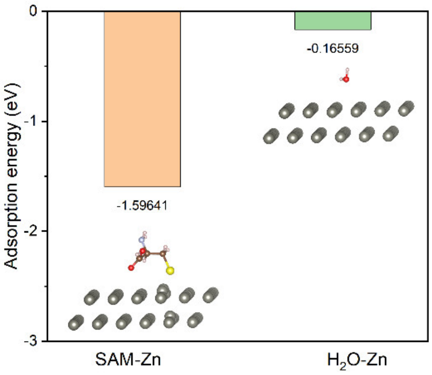

Fig. S19. Adsorption energy of SAM-Zn and H_2O-Zn.

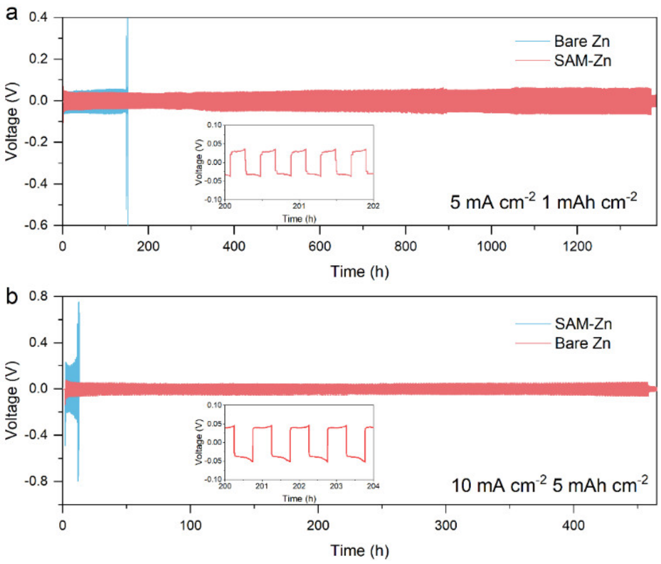

Fig. S20. Long-term cycling performance of bare Zn and SAM-Zn symmetric cells at 5 mA cm^{-2} and 10 mA cm^{-2} with a capacity of 1 mAh cm^{-2} and 5 mAh cm^{-2}, respectively.

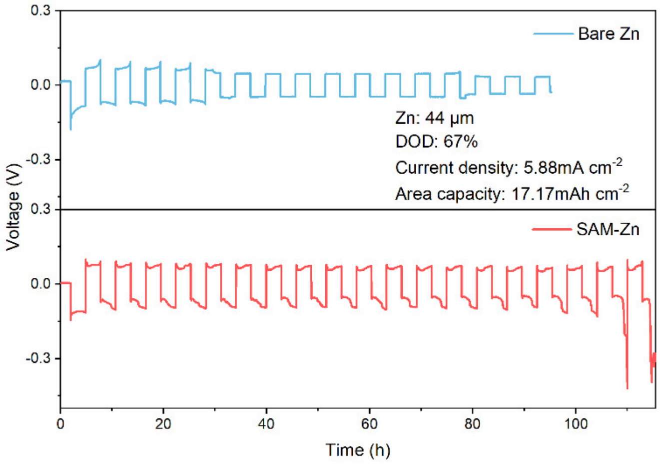

Fig. S21. Long-term cycling performance of bare Zn and SAM-Zn symmetric cells at 5.88 mA cm^{-2} with a capacity of 17.17 mAh cm^{-2}.

The symmetrical cell with SAM-Zn shows a prolonged lifespan of 109 h even under the severe condition of 67% DOD. In contrast, the bare Zn only lasted 27 h at a current density of 5.88 mA cm^{-2} with a capacity of 17.17 mAh cm^{-2}.

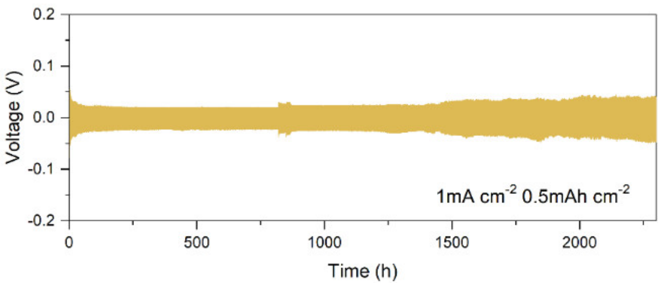

Fig. S22. Long-term cycling performance of SAM-Zn sonicated for 30 min symmetric cells at 1 mA cm^{-2} with a capacity of 0.5 mAh cm^{-2}

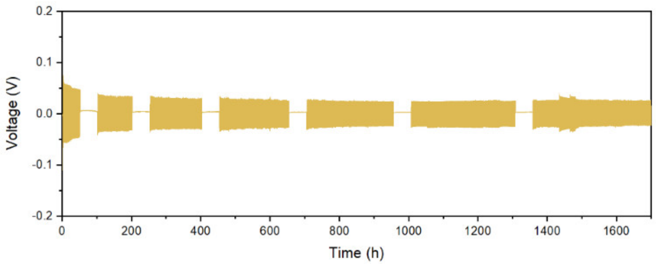

Fig. S23. Dynamic alternating cycle (50×2^{n-1} h, where n is the number of test cycles)-resting measurement (50 h per cycle) of SAM-Zn.

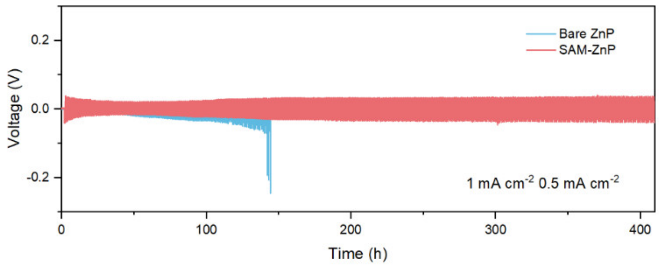

Fig. S24. Long-term cycling performance of bare ZnP and SAM-ZnP.

SAM-Zn powder (SAM-ZnP) and pristine Zn powder electrodes symmetric cells were assembled to measure the reversibility of Zn plating/stripping (depth of discharge (DOD): 14.1%). Unlike isotropic 2D Zn foils without electronic transitions in radial and lateral barriers, monodisperse 3D Zn powders are more challenging due to longer redistribution pathways of Zn ions, more extensive nucleation, and incoherent electronic transitions.[1] The polarization potential of zinc foil electrode drops rapidly due to a short circuit, while the zinc powder electrode suffers from electrical contact failure.[2] Without the protection of the artificial layer, the bare ZnP cell demonstrates a sudden rise in voltage polarization after ~140 h, which could be attributed to the "tip effect" and incoherent electronic transitions induced by monodisperse 3D inhomogeneous deposition. In contrast, the symmetric SAM-ZnP cell exhibits a conspicuous lifespan of over 400 h with low and extremely stable voltage hysteresis during the whole long-term cycling, manifesting this strategy is also suitable for stabilizing zinc powder electrodes.

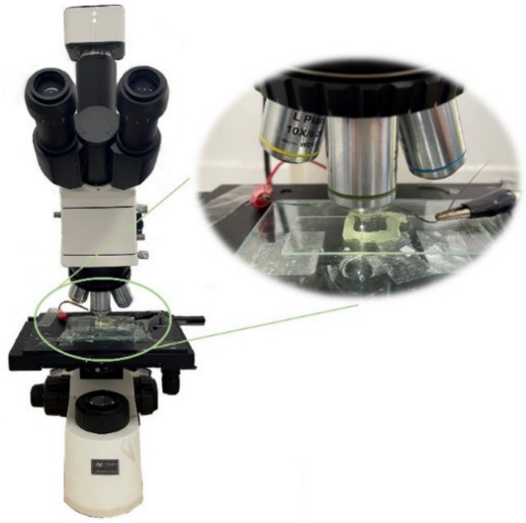

Fig. S25. The schematic diagram of optical Zn (SAM-Zn) and cell for *in situ* Zn dendrite observation.

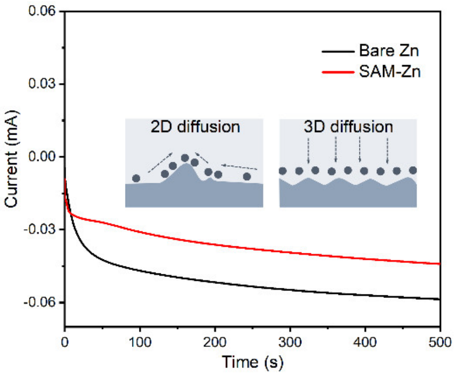

Fig. S26. Chronoamperometry (CA) curves of bare Zn and SAM-Zn at a constant potential of -150 mV.

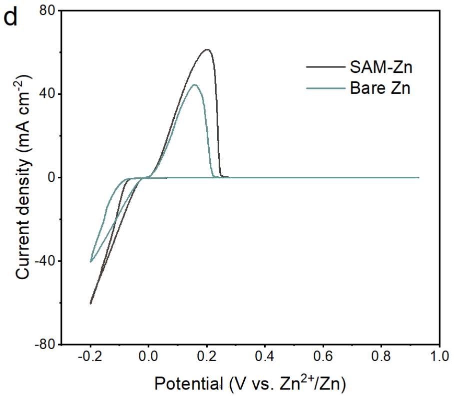

Fig. S27. CV curves of the Cu||bare Zn and Cu||SAM-Zn cells.

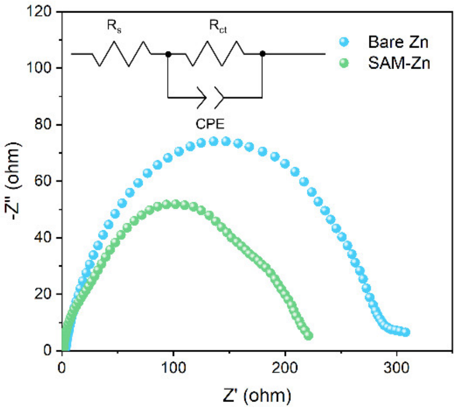

Fig. S28. EIS of bare Zn and SAM-Zn.

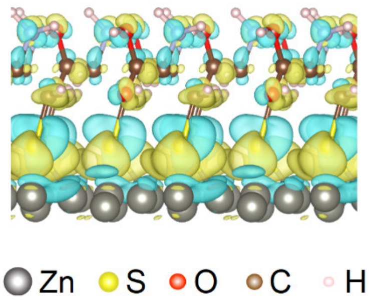

Fig. S29. Calculations of charge density distributions.

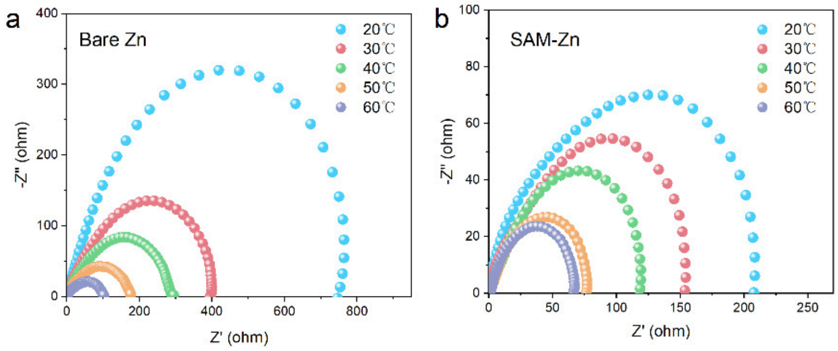

Fig. S30. EIS of bare Zn and SAM-Zn symmetric cells at different temperatures.

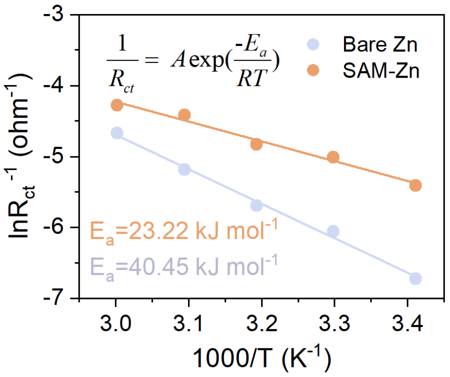

Fig. S31. The calculated desolvation activation energies of bare Zn and SAM-Zn by using the Arrhenius equation.

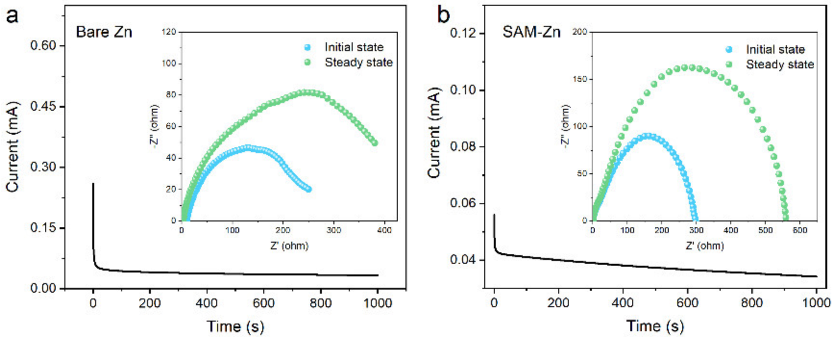

Fig. S32. CA measurement result and EIS results before and after CA measurement of a) bare Zn and b) SAM-Zn electrode.

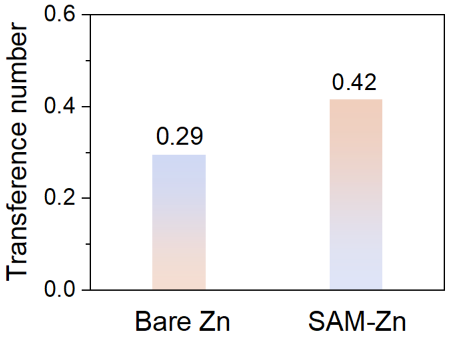

Fig. S33. Zn^{2+} transfer number of bare Zn and SAM-Zn.

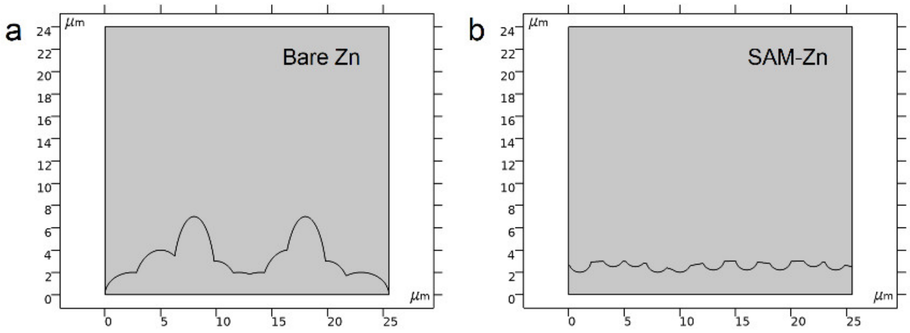

Fig. S34. Models for a) bare Zn and b) SAM-Zn electrodes.

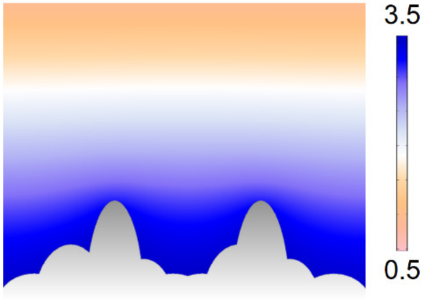

Fig. S35. Schematic illustration of Zn ion flux distribution on bare Zn.

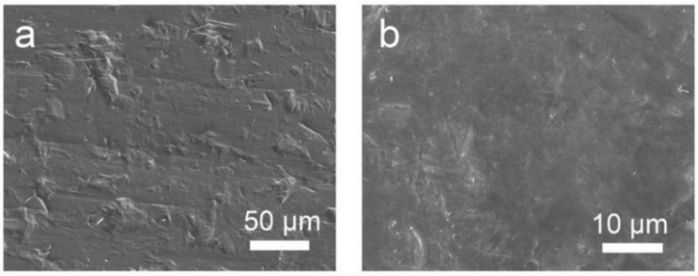

Fig. S36. SEM images of ODT@Zn.

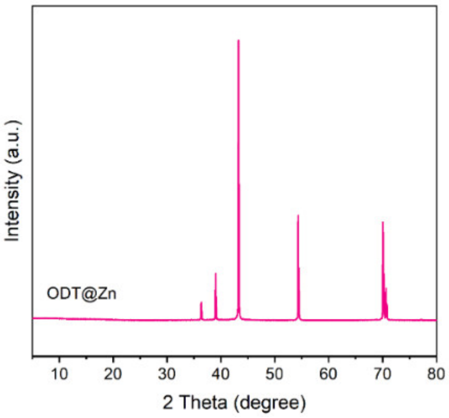

Fig. S37. XRD pattern of ODT@Zn.

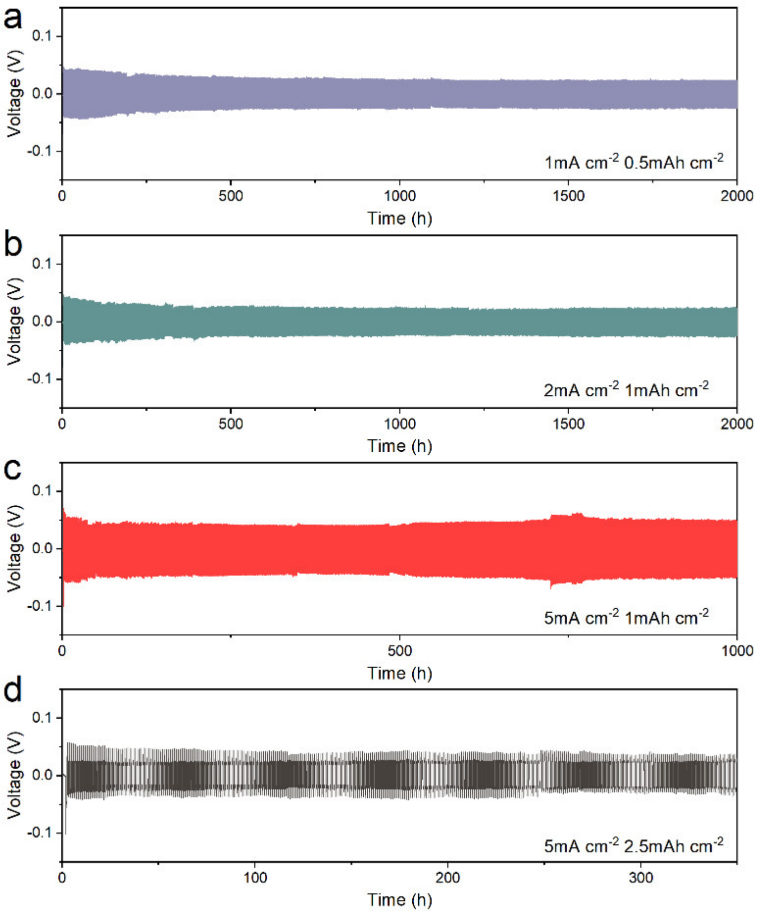

Fig. S38. Long-term cycling performance of ODT@Zn.

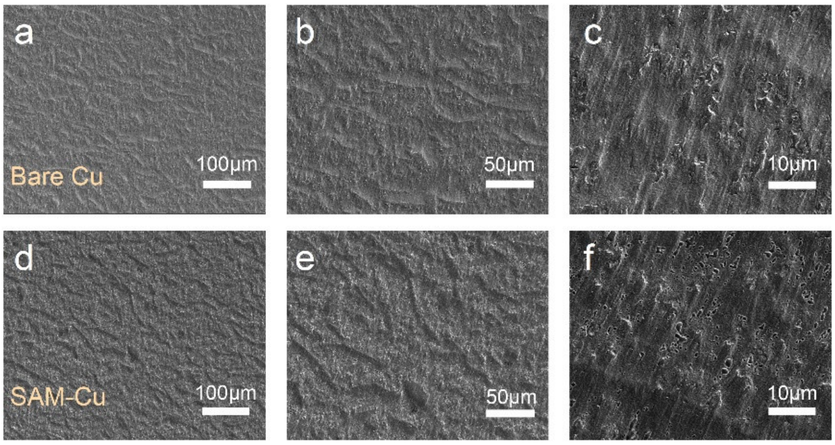

Fig. S39. SEM images of Bare Cu and SAM-Cu.

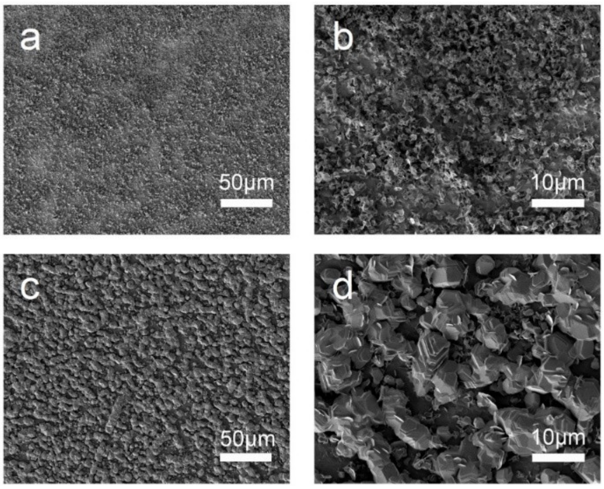

Fig. S40. SEM images of a, b) Bare Cu and c, d) SAM-Cu electrodeposited at 5 mA cm^{-2} for 10 min.

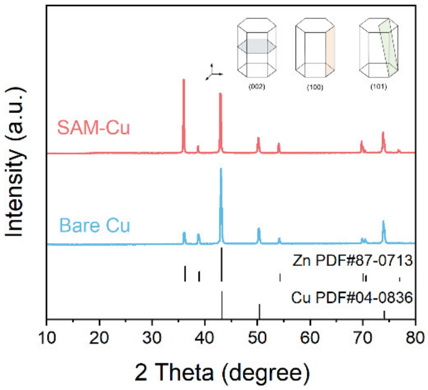

Fig. S41. XRD patterns of Bare Cu and SAM-Cu electrodeposited at 5 mA cm^{-2} for 10 min.

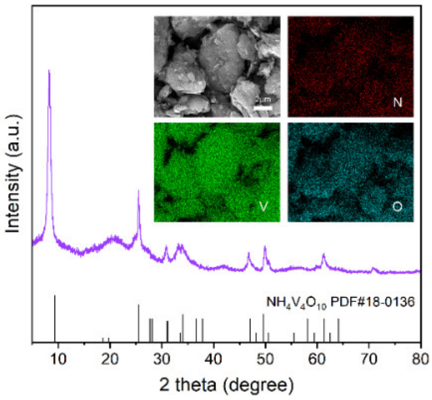

Fig. S42. XRD pattern, SEM image and EDS of $NH_4V_4O_{10}$ powder.

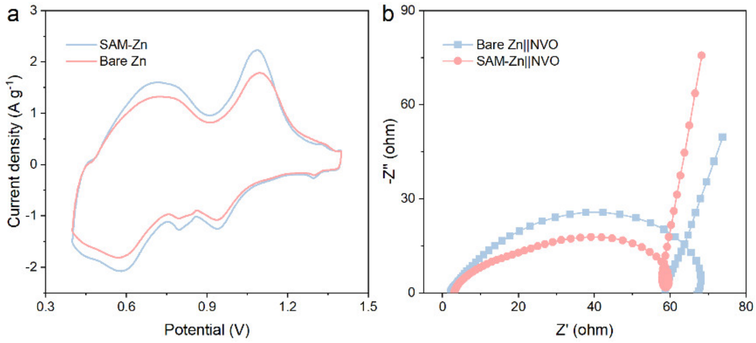

Fig. S43. a) CV curves at 1 mV s^{-1} and b) EIS of bare Zn||NH$_4$V$_4$O$_{10}$ and SAM-Zn||NH$_4$V$_4$O$_{10}$.

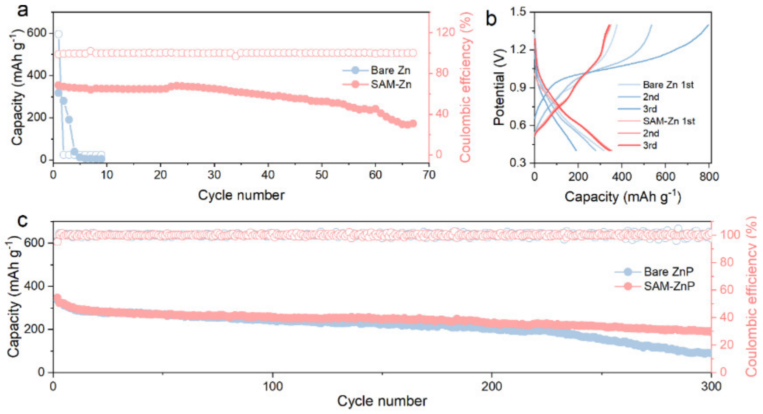

Fig. S44. a) Long-term cycling performance of bare Zn||NH$_4$V$_4$O$_{10}$ and SAM-Zn||NH$_4$V$_4$O$_{10}$ at 0.5 A g^{-1} (N:P ratio=3.2). b) Charge and discharge curves of the bare Zn||NH$_4$V$_4$O$_{10}$ and SAM-Zn||NH$_4$V$_4$O$_{10}$. c) Long-term cycling performance of bare ZnP||NH$_4$V$_4$O$_{10}$ and SAM-ZnP||NH$_4$V$_4$O$_{10}$ at 5 A g^{-1} (N:P ratio=7.0).

Table S1. Comparison of cyclic reversibility of the recent reports.

Anode	Electrolyte	Current density (mA cm^{-2})	Capacity (mAh cm^{-2})	CPC (mAh cm^{-2})	Ref.
Zn-PA@Zn	2 M $ZnSO_4$	0.5	0.25	1000	3
ZnGaIn//MXene	2 M $ZnSO_4$	1	1	600	4
PCu@Zn	2 M $ZnSO_4$	10		2000	5
N/Se-MXene@ZnSe@Zn	2 M $ZnSO_4$	5	5	3500	6
Zn/ex-ZrP	2 M $ZnSO_4$	6	3	2700	7
TpPa-SO_3H@Zn	1 M $ZnSO_4$	1	5	1000	8
PDMS/TiO_{2-x}@Zn		1	1	900	9
$KMnO_4$ treated Zn	2 M $ZnSO_4$	5	5	425	10
MXene-mPPy/Zn	2 M $ZnSO_4$	0.2	0.2	500	11
Zn@CuNW	2 M $ZnSO_4$	5	2.5	1250	12
MCM41-Zn	3 M $ZnSO_4$	1	1	1800	13
NFZP@Zn	1 M $Zn(CF_3SO_3)_2$	2	1	1800	14
TFA-AN@Zn	1 M $ZnSO_4$	4	2	1500	15
TiN (200)@Zn	2 M $ZnSO_4$	5	0.5	2500	16
MXene-coated Zn	2 M $ZnSO_4$	0.2	0.2	164	17
SAM-Zn	2 M $ZnSO_4$	1	0.5	2500	This work
SAM-Zn	2 M $ZnSO_4$	5	1	6850	This work
SAM-Zn	2 M $ZnSO_4$	10	5	4600	This work

Table S2. Simulated impedance parameters of Nyquist plots of bare Zn and SAM-Zn.

	R_s (Ω)	R_{ct} (Ω)	CPE (μΩ S^n cm^{-2})	n	C_{dl} (μF cm^{-2})
Bare Zn	1.771	286	286.55	0.61532	71.47
SAM-Zn	1.116	215	543.98	0.55607	98.07

References

1. Q. Li, Y. Wang, F. Mo, D. Wang, G. Liang, Y. Zhao, Q. Yang, Z. Huang and C. Zhi, *Adv. Energy Mater.*, 2021, **11**, 2003931.
2. X. Li, Q. Li, Y. Hou, Q. Yang, Z. Chen, Z. Huang, G. Liang, Y. Zhao, L. Ma, M. Li, Q. Huang and C. Zhi, *ACS Nano*, 2021, **15**, 14631-14642.
3. H. Liu, J. Wang, W. Hua, L. Ren, H. Sun, Z. Hou, Y. Huyan, Y. Cao, C. Wei and F. Kang, *Energy Environ. Sci.*, 2022, **15**, 1872-1881.
4. J. Gu, Y. Tao, H. Chen, Z. Cao, Y. Zhang, Z. Du, Y. Cui and S. Yang, *Adv. Energy Mater.*, 2022, **12**, 2200115.
5. J. Zhou, F. Wu, Y. Mei, Y. Hao, L. Li, M. Xie and R. Chen, *Adv. Mater.*, 2022, **34**, 2200782.
6. Y. Tian, Y. An, Y. Yang and B. Xu, *Energy Storage Mater.*, 2022, **49**, 122-134.
7. H. Peng, C. Liu, N. Wang, C. Wang, D. Wang, Y. Li, B. Chen, J. Yang and Y. Qian, *Energy Environ. Sci.*, 2022, **15**, 1682-1693.
8. J. Zhao, Y. Ying, G. Wang, K. Hu, Y. D. Yuan, H. Ye, Z. Liu, J. Y. Lee and D. Zhao, *Energy Storage Mater.*, 2022, **48**, 82-89.
9. Z. Guo, L. Fan, C. Zhao, A. Chen, N. Liu, Y. Zhang and N. Zhang, *Adv. Mater.*, 2022, **34**, 2105133.
10. P. He and J. Huang, *Adv. Mater.*, 2022, **34**, 2109872.
11. Y. Zhang, Z. Cao, S. Liu, Z. Du, Y. Cui, J. Gu, Y. Shi, B. Li and S. Yang, *Adv. Energy Mater.*, 2022, **12**, 2103979.
12. S. Xie, Y. Li, X. Li, Y. Zhou, Z. Dang, J. Rong and L. Dong, *Nano-Micro Letters*, 2021, **14**, 39.
13. Z. Miao, F. Zhang, H. Zhao, M. Du, H. Li, H. Jiang, W. Li, Y. Sang, H. Liu and S. Wang, *Adv. Funct. Mater.*, 2022, **32**, 2111635.
14. S. Wang, Z. Yang, B. Chen, H. Zhou, S. Wan, L. Hu, M. Qiu, L. Qie and Y. Yu, *Energy Storage Mater.*, 2022, **47**, 491-499.
15. W. Wang, G. Huang, Y. Wang, Z. Cao, L. Cavallo, M. N. Hedhili and H. N. Alshareef, *Adv. Energy Mater.*, 2022, **12**, 2102797.
16. J. Zheng, Z. Cao, F. Ming, H. Liang, Z. Qi, W. Liu, C. Xia, C. Chen, L. Cavallo, Z. Wang and H. N. Alshareef, *ACS Energy Lett.*, 2021, **7**, 197-203.
17. N. Zhang, S. Huang, Z. Yuan, J. Zhu, Z. Zhao and Z. Niu, *Angew. Chem. Int. Ed. Engl.*, 2021, **60**, 2861-2865.